

Bio-Inspired Retina by Regulating Ion-Confined Transport in Hydrogels

Hongjie Zhang, Song Wang, Li Wang,* Shengke Li, Haowen Liu, Xinyi Zhu, Yuanxia Chen, Guoheng Xu, Mingming Zhang, Quanying Liu,* Ruibing Wang,* and Kai Xiao*

The effective and precise processing of visual information by the human eye primarily relies on the diverse contrasting functions achieved through synaptic regulation of ion transport in the retina. Developing a bio-inspired retina that uses ions as information carriers can more accurately replicate retina's natural signal processing capabilities, enabling high-performance machine vision. Herein, an ion-confined transport strategy is proposed to construct a bio-inspired retina by developing artificial synapses with inhibitory and excitatory contrasting functions. By fine-tuning the ionic hydrogel structures to control ion transport across the heterogeneous interfaces, inhibitory and excitatory synapses are realized to negatively or positively modulate the optical signal. The integration of these synapses facilitates advanced tasks such as image recognition and motion analysis. Moreover, as a proof of concept, guiding robot vehicles to perform path planning is demonstrated. This work offers a new idea for constructing the bio-inspired retina by precisely regulating ion transport, allowing it to reach a level closer to the biological retina.

and dim light,^[1] ON and OFF types of bipolar cells respond differently to changes in light intensity,^[2] and magnocellular and parvocellular cells in ganglion cells have different sensitivities to low-contrast and high-contrast optical information.^[3] These contrasting mechanisms of retinal cells primarily rely on the collaboration of inhibitory and excitatory synapses, which regulate neuronal activity through various ion channels.^[4] Inhibitory synapses decrease postsynaptic potentials (PSP) by opening chloride channels, thereby generating inhibitory PSP (IPSP).^[5] This can attenuate unwanted or noisy signals and regulate visual signal transmission. Conversely, excitatory synapses increase the PSP by opening sodium and calcium channels, resulting in the excitatory PSP (EPSP).^[6] This amplification of signals can enhance the contrast and sharpness of image information

1. Introduction

The various biological components with contrasting functions in the retina form the foundation of visual perception. Specifically, cone cells and rod cells are respectively sensitive to bright light

(Figure 1A). The diverse and tunable ion transport behaviors allow the visual system to precisely distinguish changes in light, facilitating efficient visual information processing. Inspired by biological retina, visual processing platforms based on neuromorphic devices have made significant progress.^[7] These platforms perform synaptic functions with electrons as carriers, achieving feature extraction,^[8] image processing,^[9] and motion tracking functions.^[10] However, compared to biological systems that use ions as charge carriers, these methods exhibit less regulatory diversity and may face challenges related to signal mismatch.^[11]

Over the past decade, scientists have been exploring the material systems and construction methods of ionic artificial synapses,^[12] particularly focusing on nanofluidic memristors inspired by ion channels. These devices regulate ion transport through the spatial confinement effect in nano- and sub-nano pores or channels, achieving modulation and memory of conductance. Among these efforts, various nanofluidic memristors have been constructed with different channel structures to confine ion transport behavior, which can be used for storing information,^[13] constructing logic circuits,^[14] and implementing neuromorphic computing,^[15] etc. However, the electrochemical performance of nanofluidic devices highly relies on the precise fabrication of channel structures, and using fluids as ion reservoirs hinders miniaturization and large-scale integration.^[16] Ion-conducting gels exhibit excellent ion transport properties and can be miniaturized and integrated through micro-nano

H. Zhang, S. Li, R. Wang
State Key Laboratory of Quality Research in Chinese Medicine
Institute of Chinese Medical Sciences
University of Macau
Taipa, Macau, SAR 999078, P. R. China
E-mail: rwang@um.edu.mo

H. Zhang, S. Wang, L. Wang, H. Liu, X. Zhu, Y. Chen, G. Xu, M. Zhang, Q. Liu, K. Xiao
Department of Biomedical Engineering
Guangdong Provincial Key Laboratory of Advanced Biomaterials
Institute of Innovative Materials
Southern University of Science and Technology
Shenzhen 518055, P. R. China
E-mail: 1260524832@qq.com; liuqy@sustech.edu.cn; xiaok3@sustech.edu.cn

L. Wang
School of Chemistry and Molecular Engineering
Nanjing Tech University
Institute of Innovative Materials
Southern University of Science and Technology
Nanjing 211816, P. R. China

 The ORCID identification number(s) for the author(s) of this article can be found under <https://doi.org/10.1002/adma.202500809>

DOI: 10.1002/adma.202500809

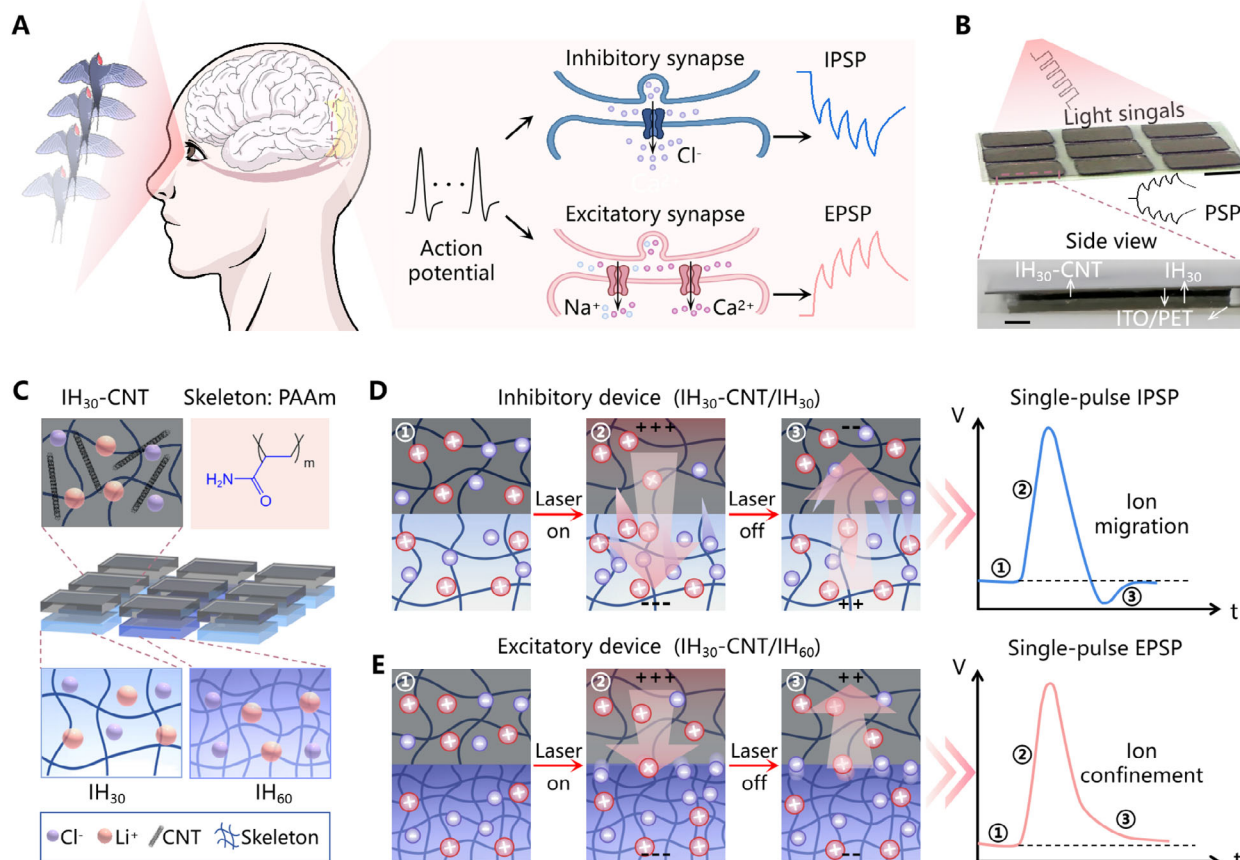


Figure 1. Bio-inspired retina by regulating ion-confined transport in hydrogel for visual information processing. A) Schematic of human visual system for processing both image and motion information. B) Photographs of bio-inspired retina with inhibitory and excitatory hydrogel artificial synapses for optical signal processing. In the figure above, the scale bar represents 0.3 cm. The size of device is 0.5 cm × 0.5 cm. The scale of the enlarged side view is 0.5 mm, and the thickness of the device is 0.8 mm. C) Chemical structures of the polymer skeletons of IH₃₀-CNT, IH₃₀ and IH₆₀ layers. D) Schematic diagram of the ion transport mechanism in inhibitory devices (IH₃₀-CNT/IH₃₀). E) Schematic diagram of the ion transport mechanism in excitatory devices (IH₃₀-CNT/IH₆₀).

processing technology,^[17] making them ideal materials for constructing flexible and biocompatible visual processing platforms. Furthermore, recent studies have demonstrated that controlling ion migration within gels can emulate short-term potentiation (STP)^[18] and long-term potentiation (LTP)^[19] of biological synapses, enabling learning and memory functions. Although these studies have established a strong basis for controlling ion transport, they are limited to simulating a particular synapse (inhibitory synapse or excitatory synapse). Consequently, building ionic bio-inspired retinas with contrasting functions remains a significant challenge.

Herein, we developed a bio-inspired retina based on bilayer ionic hydrogel synaptic devices. By adjusting the structures of the hydrogels to confine ion transport, inhibitory and excitatory contrasting functions were achieved. When both hydrogel layers are sparse, the larger network pores allow ions to migrate freely across the heterogeneous interface, creating inhibitory artificial synapses. In contrast, when the bottom hydrogel layer is denser than the upper layer, the network pores become narrower, increasing the resistance to ion movement at the interface due to steric effects.^[20] The resulting interface barrier confines ion transport, forming excitatory artificial synapses. This

contrasting regulation mechanism of inhibitory and excitatory synapses enables effective dynamic regulation and processing of image signals. Inhibitory hydrogel artificial synapses weaken the transmission of light signals, while excitatory hydrogel artificial synapses enhance it, facilitating information storage for short-term processing and adaptation. By integrating inhibitory and excitatory artificial synapses into convolutional kernels, tasks typical of a bio-inspired retina, such as edge detection, sharpening, and noise reduction, were successfully demonstrated. Moreover, the biomimetic motion detector with excitatory artificial synapses can achieve direction recognition and path analysis. Additionally, these devices can guide a robot vehicle in performing path planning. This work provides an efficient solution for realizing intelligent bio-inspired retina.

2. Results and Discussion

2.1. Hydrogel Artificial Synapses with Inhibitory and Excitatory Contrasting Functions

The hydrogel artificial synapses are composed of bilayer ionic hydrogel containing 0.1 M lithium chloride (LiCl) and two indium

tin oxide/polyethylene terephthalate (ITO/PET) electrodes covering the hydrogel's top and bottom surfaces (Figure 1B). The structure of ionic hydrogel can be adjusted by changing the solid content, denoted as IH_x , where x represents the mass percentage of polyacrylamide (Figure 1C). Figure S1 (Supporting Information) presents the morphology of IH_{30} and IH_{60} hydrogels. It can be observed that the higher solid content in IH_{60} leads to a narrower pore structure, while IH_{30} exhibits a more open network structure. Synthesis and device construction process are detailed in Methods section. The ionic hydrogel possesses soft elasticity and high water content, facilitating the movement of lithium ions (Li^+) and chloride ions (Cl^-). By introducing carbon nanotube (CNT) into the upper hydrogel (named IH_{30} -CNT), its color changes from transparent to black, resulting in broadband absorption in the ultraviolet-visible-near infrared (UV-vis-NIR) region (Figure S2, Supporting Information). The doped CNTs are a few micrometers long, with a tube diameter of 5 nm, as shown in the TEM and high-resolution TEM images (Figure S3, Supporting Information). This modification enhances the hydrogel's ability to absorb light across a wide spectrum. CNT is known for its excellent photothermal properties, effectively converting laser irradiation into heat within the UV-vis-NIR region (Figure S4, Supporting Information). This photothermal conversion can generate a significant temperature gradient within heterogeneous hydrogels, which drives ion migration due to the Soret effect.^[21] By modulating the structure of the bottom hydrogel, inhibitory artificial synapses (IH_{30} -CNT/ IH_{30}) and excitatory artificial synapses (IH_{30} -CNT/ IH_{60}) can be respectively prepared to achieve contrasting functions in the bio-inspired retina. In the inhibitory device, Cl^- rapidly migrates to the IH_{30} layer under laser exposure due to the difference in migration rates of anions and cations,^[22] creating an uneven ion distribution and generating an ionic potential. When the laser is turned off, Cl^- rapidly diffuses to the IH_{30} -CNT layer driven by the concentration gradient, while the slow return of Li^+ results in a potential lower than the initial value (Figure 1D). The entire process produces biosimilar IPSP that makes the PSP more negative, achieving negative signal regulation. For the excitatory synapse, under laser irradiation, rapid migration of Cl^- leads to an increase in ionic potential. However, the dense structure of the IH_{60} layer creates narrow network pores, which confine ion transport and add resistance to their movement through the interface. When the laser is turned off, both anions and cations slowly return to their initial positions across the heterogeneous interface, and the ionic potentials gradually recover to the initial value (Figure 1E). The entire process produces biosimilar EPSP, resulting in a more positive PSP and achieving positive signal regulation.

2.2. Mechanisms of Inhibitory and Excitatory Contrasting Functions

To verify the ability of the hydrogel artificial synapse to modulate light signals, we first performed the photothermal conversion experiment. As shown in Figure 2A, the temperature of IH_{30} changes little under laser irradiation. In contrast, in IH_{30} -CNT, the CNT can effectively convert laser irradiation into heat, with a photothermal conversion efficiency as high as 88% (Figure S5,

Supporting Information). A light response experiment was performed to verify the ability of the hydrogel artificial synapse to modulate light signals. When a single light pulse (power density: 0.4 W cm^{-2} , duration: 1 s) was applied to the artificial synapses, both the inhibitory and excitatory synapses produced significant positive potential. But at the end of the laser irradiation, the inhibitory device produced PSP that was lower than the initial value, exhibiting the IPSP (Figure 2B), while the excitatory device generated PSP that remained higher than the initial value, exhibiting the EPSP (Figure 2C), which is similar to the contrasting regulation mechanism of synapses in biological retina. In addition, after the laser irradiation, the PSP of both devices showed a relaxation time of several minutes, providing time-related spatial information.

To further explore the mechanism of contrasting functions by regulating ion-confined transport in the hydrogel, we performed finite element method (FEM) simulation (see Note S1, Supporting Information for modeling theory and methods), and the geometric modeling is shown in Figure S6 (Supporting Information). First, the simulation results of the temperature field indicate that the laser irradiation (turned on at 1 s) can cause a significant temperature gradient in the device, especially in the vertical direction (Figure 2D; Figure S7, Supporting Information). After the laser is turned off (at 2 s), the temperature gradually returns to equilibrium and the temperature gradient disappears. Further, the transport behavior of ions was analyzed. The results show that varying bottom structures lead to different fluxes of Cl^- and Li^+ across the interface. For the inhibitory device, the upper and bottom structures are sparse, allowing ions to move freely. The temperature gradient generated by laser irradiation promotes the migration of ions across the interface. Since the hydration radius of a Cl^- is smaller than that of a Li^+ , more Cl^- can cross the interface more quickly^[22] (Figure S8, Supporting Information). When the laser is switched off, the Cl^- and Li^+ return, with Cl^- still returning faster than the Li^+ , resulting in a reversal of the concentration ratio of Li^+ and Cl^- in the bottom and top layers of the IH at a given point in time (Figure 2E). The bottom interfacial barrier resulting from the same sparse structure allows ions to move freely based on their intrinsic properties, leading to the generation of IPSP as shown in Figure 2B (Figure S9, Supporting Information). In the case of the excitatory device, the bottom structure is denser than the upper structure, confining the transport of ions, so the temperature gradient generated by the laser irradiation only allows a small number of ions to cross the interface (Figure S10, Supporting Information). When the laser is turned off, both Cl^- and Li^+ slowly reflux simultaneously (Figure 2F). The denser structure in the bottom layer creates a higher interfacial barrier, hindering the free migration of ions. This ion-confined transport results in the generation of EPSP as shown in Figure 2C (Figure S11, Supporting Information). According to the Poisson equation for electrostatic potential,^[23] the free migration of ions in inhibitory devices leads to a reversal of the potential direction (Figure 2G; Movies S1 and S2, Supporting Information). In excitatory device, the confined transport of ions maintains the same potential direction (Figure 2H; Movie S3, Supporting Information). Eventually, the slow recovery of the ion distribution leads to potential relaxation. Figure 2I shows the simulated potential-time curve, which closely matches the experimental results.

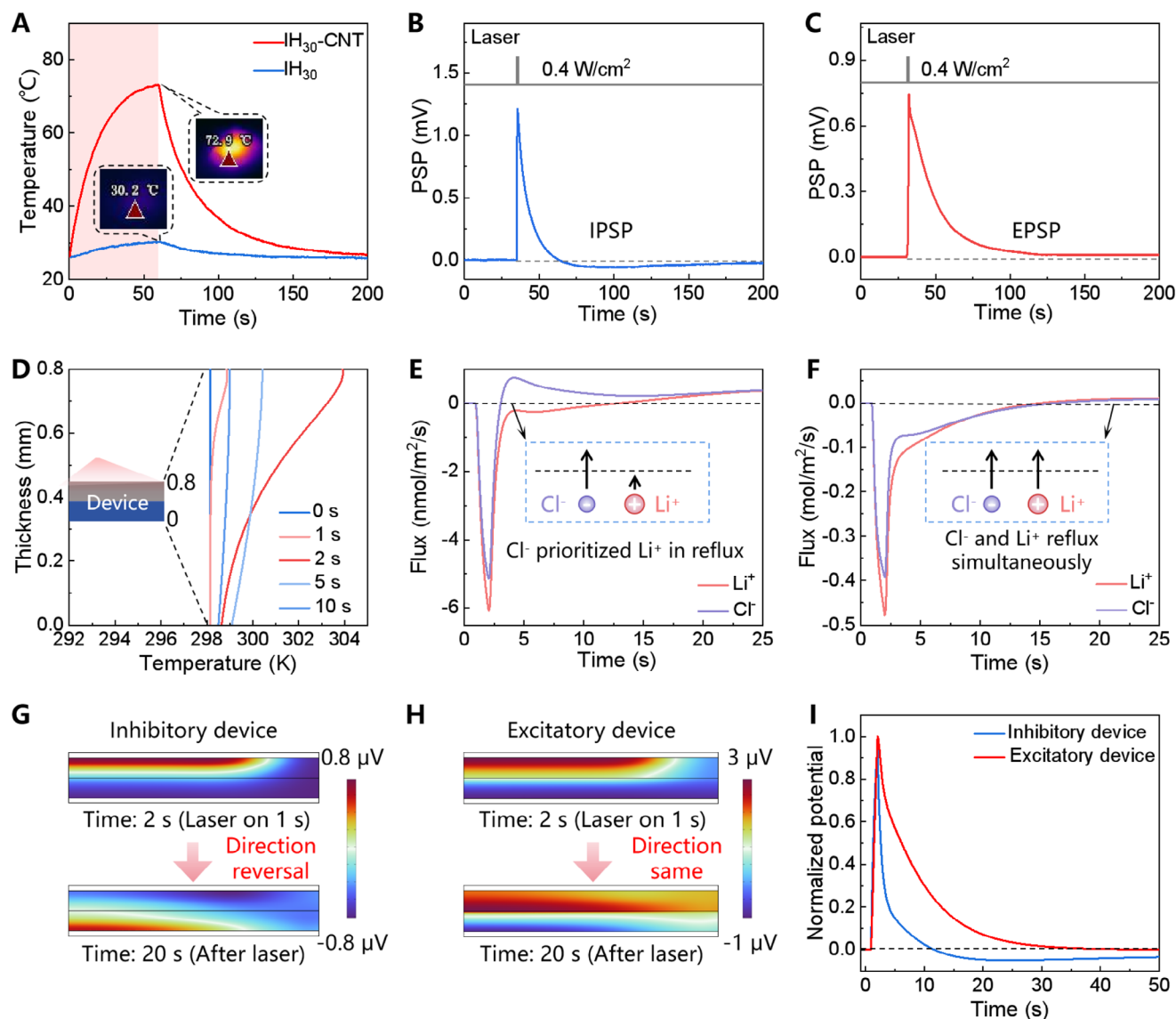


Figure 2. Mechanisms of inhibitory and excitatory contrasting functions. A) Heating and cooling curves of $\text{IH}_{30}\text{-CNT}$ and IH_{30} under 808 nm laser irradiation. B) IPSP generated by an inhibitory device exposed to 808 nm laser irradiation. C) EPSP generated by an excitatory device exposed to 808 nm laser irradiation. D) Temperature gradient within inhibitory devices under laser irradiation (simulation results). E) For inhibitory devices, the flux of chloride and lithium ions (Cl^- and Li^+) across the interface as a function of laser irradiation time (simulation results). F) For excitatory devices, the flux of Cl^- and Li^+ across the interface as a function of laser irradiation time (simulation results). G) Potential maps at the longest laser irradiation time (1s) and 20s after turning off the laser for the inhibitory device (simulation results). The bottom potential variation graph is magnified 100 times for clearer visualization. H) Potential maps at the longest laser irradiation time (1s) and 20s after turning off the laser for the excitatory device (simulation results). The bottom potential variation graph is magnified 10 times for clearer visualization. I) The normalized potential signals of inhibitory and excitatory devices induced by 808 nm laser irradiation, simulated by FEM.

2.3. Synaptic Characteristics and Neuromorphic Imaging

To verify the synaptic behavior of artificial synapses, we performed photostimulation experiments on synaptic devices under different conditions. In both inhibitory and excitatory devices, increasing the laser intensity (0.05 to 0.5 W cm^{-2}) while maintaining a 1-s laser exposure resulted in different electrical responses. It was observed that higher laser intensity led to more significant inhibition (Figure S12A, Supporting Information) and enhancement (Figure S12B, Supporting Information), respectively, ex-

hibiting spike-intensity-dependent plasticity (SIDP). Further experiments revealed the paired-pulse depression (PPD) effect, as shown in Figure 3A, by applying a pair of laser pulses. When the second pulse arrives before the full recovery of the IPSP induced by the first pulse, the cumulative effect leads to more negative IPSP. By adjusting the time interval (Δt) from 20 s to 200 s, PPD index (defined as $(A_2 - A_1)/A_1 \times 100\%$) decreased with increasing Δt , where A_1 and A_2 denote the amplitude of the first and second spike potentials, respectively (Figure S13, Supporting Information). Furthermore, we found that these decay curves could

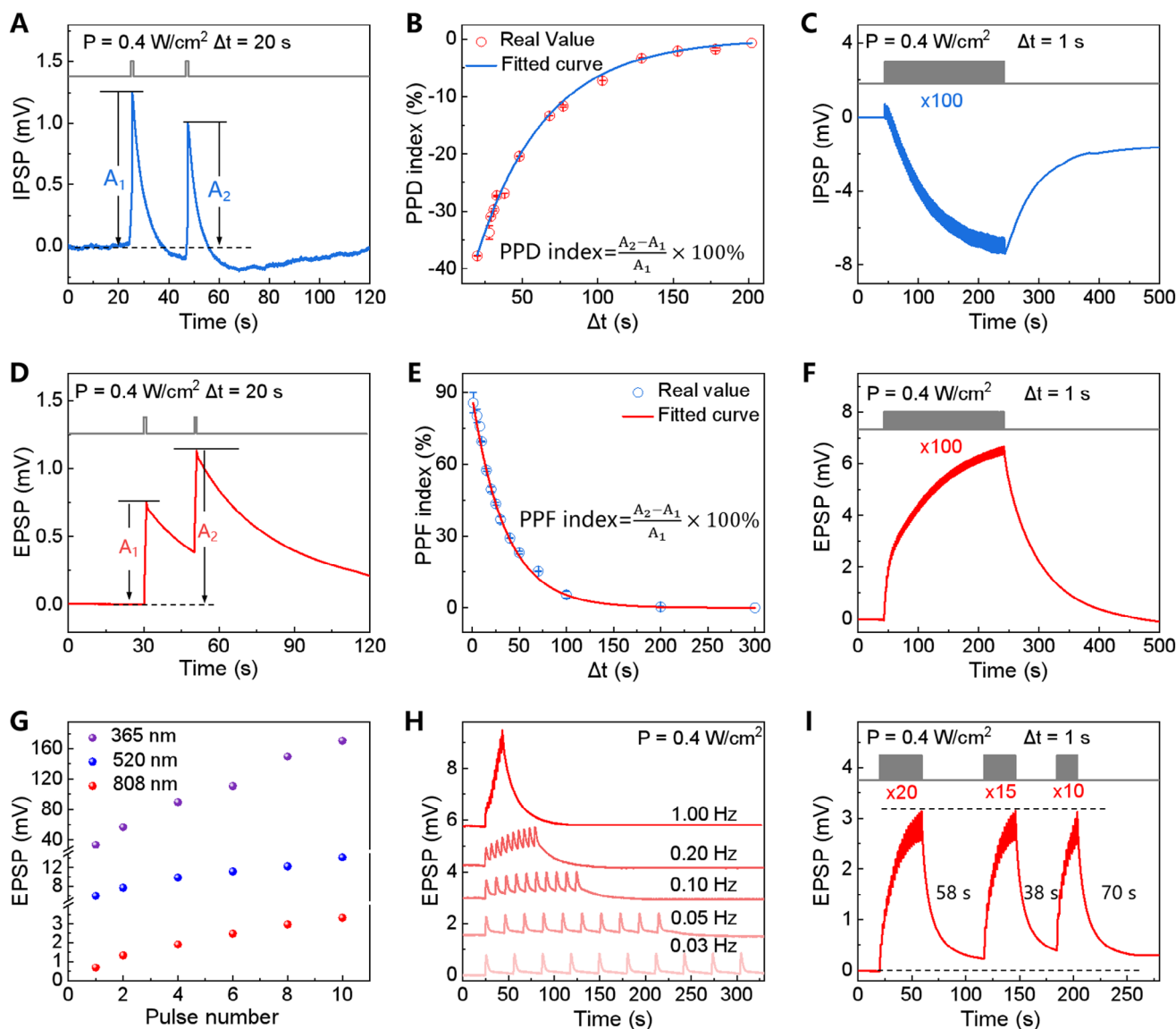


Figure 3. Synaptic characteristics of the hydrogel artificial synapses. A) PPD effect of the inhibitory device, power density (P) was 0.4 W cm^{-2} , and the time interval (Δt) between two pulsed pressure stimuli was 20 s. B) Relationship between PPD index and Δt between two stimuli, where the blue curve is the fitted bi-exponential curve (data are mean \pm SD, $N = 3$). C) LTD effect of the inhibitory device, P was 0.4 W cm^{-2} , and the Δt between two pulsed pressure stimuli was 1 s, and the stimulus number was 100. D) Relationship between PPF index and Δt between two stimuli, where the red curve is the fitted bi-exponential curve (data are mean \pm SD, $N = 3$). E) LTD effect of excitatory device, P was 0.4 W cm^{-2} , and Δt between two pulsed pressure stimuli was 1 s, and the stimulus number was 100. G) EPSP under UV–vis–NIR laser sources. H) EPSP induced by a train of optical pulses (0.4 W cm^{-2} , with frequencies of 0.03, 0.05, 0.10, 0.20, and 1 Hz). I) Learning experience behavior of excitatory device.

be well-fitted with a double exponential function (Figure 3B), which is consistent with biological synapses.^[24] In addition, under the stimulation of 100 consecutive laser pulses, the IPSP continued to decrease and showed significant memory behavior, taking $>200 \text{ s}$ to return to the initial value (Figure 3C). This signal pattern is called long-term depression (LTD). The paired-pulse facilitation (PPF) effect can also be observed by applying a pair of laser pulses (Figure 3D), where the PPF ratio (defined as $(A_2 - A_1)/A_1 \times 100\%$) increases as the Δt between pairs of spikes decreases (Figure 3E; Figure S14, Supporting Information). This result is also well-fitted with the double-exponential decay func-

tion commonly followed at biological synapses. By extending the number of pulses to 100, LTP was observed, taking $>200 \text{ s}$ to return to the initial values (Figure 3F). The width of the laser pulse used in Figure 3C,F was 1 s. These LTD/LTP effects can be attributed to the sustained accumulation of ions caused by historical laser stimulation, resulting in a continuous decrease or increase in PSP with the increase in the number of stimuli (Movies S4 and S5, Supporting Information). The simulation results also align with the experimental observations, further confirming the mechanism (Figure S15, Supporting Information). LTP enables the conversion of information from short-term memory

(STM) to long-term memory (LTM) and facilitates effective visual memory.^[25] Figure 3G illustrates EPSP across the UV–vis–NIR spectrum of excitatory artificial synapses, showing steady enhancement with increasing light pulse numbers. Inhibitory artificial synapses also exhibit light responsiveness across the same spectrum (Figure S16, Supporting Information). Figure 3H further demonstrates spike-frequency-dependent plasticity (SFDP) generated when a series of light pulses of different frequencies are applied to the device. As the spike frequency increases from 0.03 to 1 Hz, cumulative effects become more pronounced, resulting in higher EPSP responses (lower IPSP responses in inhibitory devices, Figure S17, Supporting Information). Concurrently, laser-induced PSP in hydrogel artificial synapses remains stable during 100-pulse-cycle operations (Figures S18 and S19, Supporting Information), indicating the device's robust stability. Similarly, five inhibitory devices and five excitatory devices were exposed to the same light conditions (0.4 W cm⁻², 1-s pulse width, and 1-s pulse interval) for ten cycles. The resulting PSP signals exhibited highly consistent characteristics (Figures S20, Supporting Information), further validating the excellent parallel performance of these devices.

As mentioned above, STM and LTM play key roles in image information processing. Learning is a process of memory acquisition. When learning new information, the information is first stored as STM, which has a short duration. With repeated training, some information can be transformed into LTM (Figure S21A, Supporting Information). A typical phenomenon in the learning experience is that it is usually easier to relearn forgotten memories than to learn them for the first time, known as the memory-sparing effect, which contributes to more efficient recognition for the retina. Based on the LTP characteristics of the excitatory devices, we simulated the learning-forgetting-relearning process to evaluate the effectiveness of learning (Figure 3I). During the initial learning phase, 20 laser pulses achieved 100% learning level; however, after stimulus removal, the learning level gradually declined, reflecting the forgetting process. In the relearning phase, only 15 laser pulses were needed to return to the previous level, indicating that relearning takes less time than initial learning. The third relearning phase (with 10 pulses) also exhibited a similar trend. Notably, after the third relearning, the retention time of memory information was longer than that in the initial phase, suggesting that repeated learning can enhance memory capability. It was further used for visual information storage. We prepared a 3 × 3 array of excitatory devices, with each device (pixel) serving as an independent storage unit (Figure S21B, Supporting Information). The measurement setup of the devices is shown in Figure S22 (Supporting Information) and described in detail in Note S2 (Supporting Information). We simultaneously wrote a “T-shaped” image with 5 input pulses per pixel and an “L-shaped” image with 10 input pulses per pixel onto this array. After 20 s, both images were effectively memorized but indistinguishable. After 100 s, the “T-shaped” image's memorization decreased significantly, and after 200 s, the “L-shaped” image became clear (Figure S21C, Supporting Information). This indicates that excitatory devices achieve steady sensing and memory, exhibiting the potential for image recognition.

2.4. Neuromorphic Edge Detection for Image Recognition

Edge detection is crucial in image recognition as it can simplify image data, reduce processing load, and retain key information, thereby improving the efficiency of image recognition and analysis. The retina's edge detection function primarily relies on the contrasting mechanism of the center-surround receptive field (On-center/Off-surround receptive field).^[26] This receptive field structure features central excitation and peripheral inhibition, meaning that when light is directed at the central region, bipolar cells produce an excitatory response, while light in the surrounding area induces an inhibitory response.^[27] This contrast between the center and the periphery enhances the dramatic changes in image grayscale or color, i.e., edges, making them more prominent and distinct in the visual system (Figure 4A). The Mach band effect is one of the important visual phenomena for edge detection.^[28] In a series of adjacent gray-scale bands, the human eye perceives a false luminance enhancement at the boundary of each band that appears to be more significant than the actual luminance change (Figure 4B). In our system, the Mach band effect was realized by integrating excitatory and inhibitory devices (Figure 4C; Figure S23, Supporting Information), which can be then used for edge detecting. The detailed experimental method is shown in Figure S24 (Supporting Information). By adjusting the hydrogel structure within the device, its ability to modulate light signals can be altered, enabling the implementation of convolutional kernels with different weights. Figure S25 (Supporting Information) illustrates the PSP changes in each device after training with ten consecutive laser pulses. Measurements taken 2 s after the pulses and subsequently normalized reveal weights for various edge detection kernels (−1, −2, 1, 2, 5) and noise reduction kernels (0.2, 0.125, 0.075). This approach allows for the configuration of kernels with different response distributions, achieving successful perception and processing of images, including edge detection and sharpening (Figure 4D; Figure S26, Supporting Information). And the experimental procedures are detailed in the convolutional processing method of Note S3 (Supporting Information).

To further demonstrate the effectiveness of neuromorphic edge detection in enhancing image recognition accuracy, random Gaussian noise was introduced into the MNIST dataset to simulate real-world visual interference. A visual processing platform was constructed, featuring a Gaussian kernel denoising operator simulated by a 3 × 3 synaptic device array and a two-layer linear network. A training set of 800 images and a test set of 200 images, both with Gaussian noise (mean = 0, standard deviation = 0.5), were created, covering ten classes of numbers (from “number 0” to “number 9”) from the MNIST dataset.^[29] Each 28 × 28 pixel image was preprocessed with the synaptic array model to generate a contrast-enhanced dataset, which was then classified by the two-layer linear network (detailed in the noise reduction experimental procedures of Note S3, Supporting Information). Results (Figure 4E; Figure S27, Supporting Information) show that the synaptic array preprocessing significantly reduced noise, improved image quality, and enhanced contrast between numbers and background. Notably, the contrast-enhanced dataset achieved a maximum classification accuracy of 83%

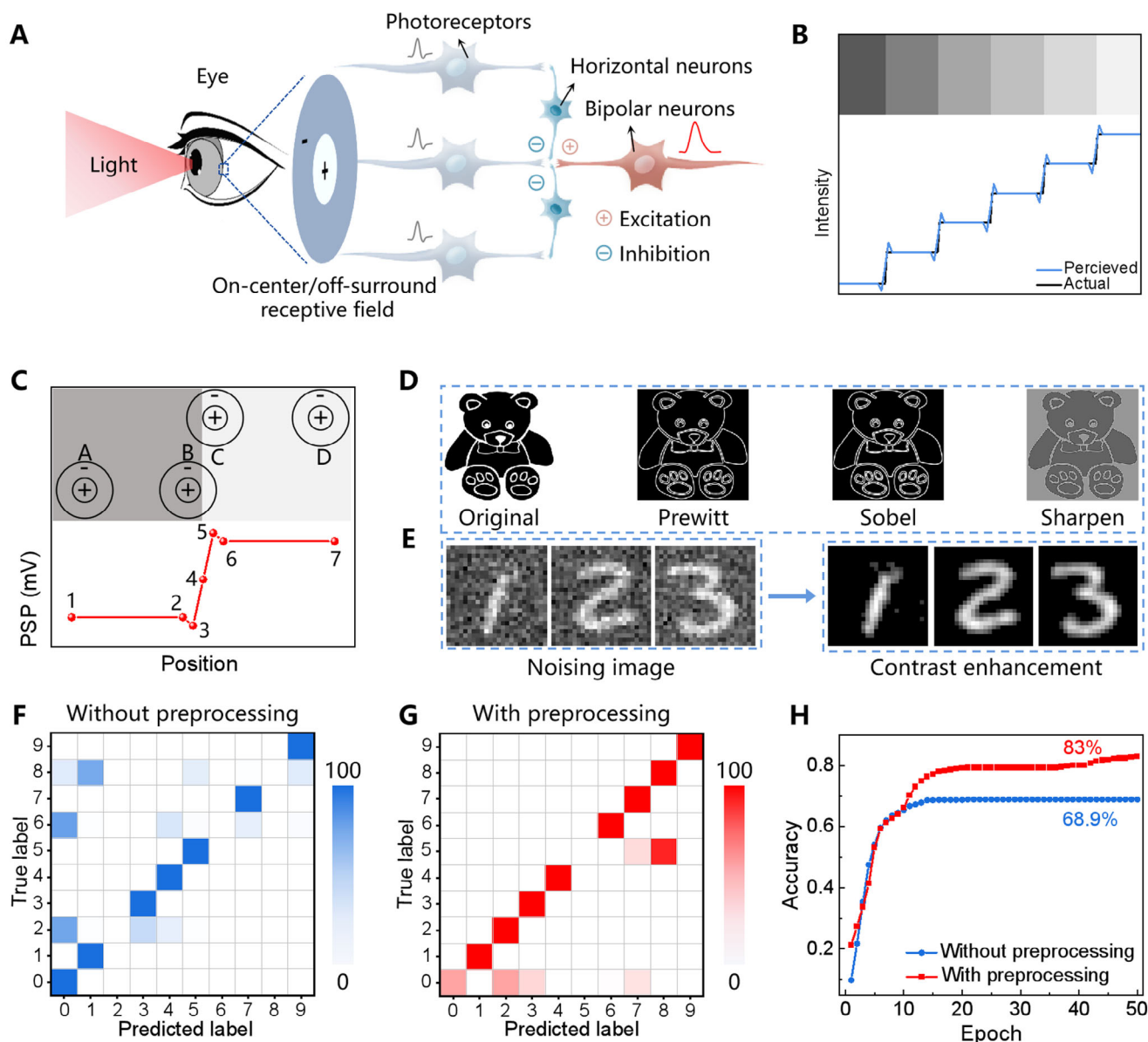


Figure 4. Edge detection and contrast enhancement functions of bio-inspired retina. A) Schematic illustration of an On-center/Off-surround receptive field in the biological retina, formed by direct excitatory connections from photoreceptors to bipolar neurons and indirect inhibitory effects from horizontal cells. B) Schematic illustration of the Mach band effect in a retina, showing the enhancing perceived contrast at the edges between regions of different gray levels. C) Implementation of the Mach band effect in our system. The numbers in the figure represent test positions 1–7. D) Demonstration of various convolutional processing operations including Prewitt edge detection, Sobel edge detection, and sharpness. E) Noising image and contrast enhancement. These images were initially corrupted with random Gaussian noise (mean = 0, standard deviation = 0.5). F) Confusion matrices of the classifications of “number 0” – “number 9” images without preprocessing. G) Confusion matrices of the classifications of “number 0” – “number 9” images with preprocessing. H) Recognition accuracies of the classifications of “number 0” – “number 9” images without and with preprocessing.

after 40 training epochs, compared to 68.9% for the denoised-only dataset after 20 training epochs (Figure 4F–H).

2.5. Visual Processing Platform for Motion Analysis and Implementation of Path Planning

The retina processes motion imaging into a compressed state of time by perceiving continuous temporal frames of motion and

using synapses to regulate and process signals, thereby achieving motion perception and imaging (Figure 5A). The potential relaxation properties of the hydrogel artificial synapse enable it to encode temporal information in a sequential manner. Furthermore, the relaxation properties in excitatory artificial synapses can be effectively modulated by adjusting the number of laser pulses, allowing for experimental implementation of analysis for moving targets. Figure 5B shows the decay characteristics of excitatory devices after training with 1 to 20 consecutive light pulses. As the

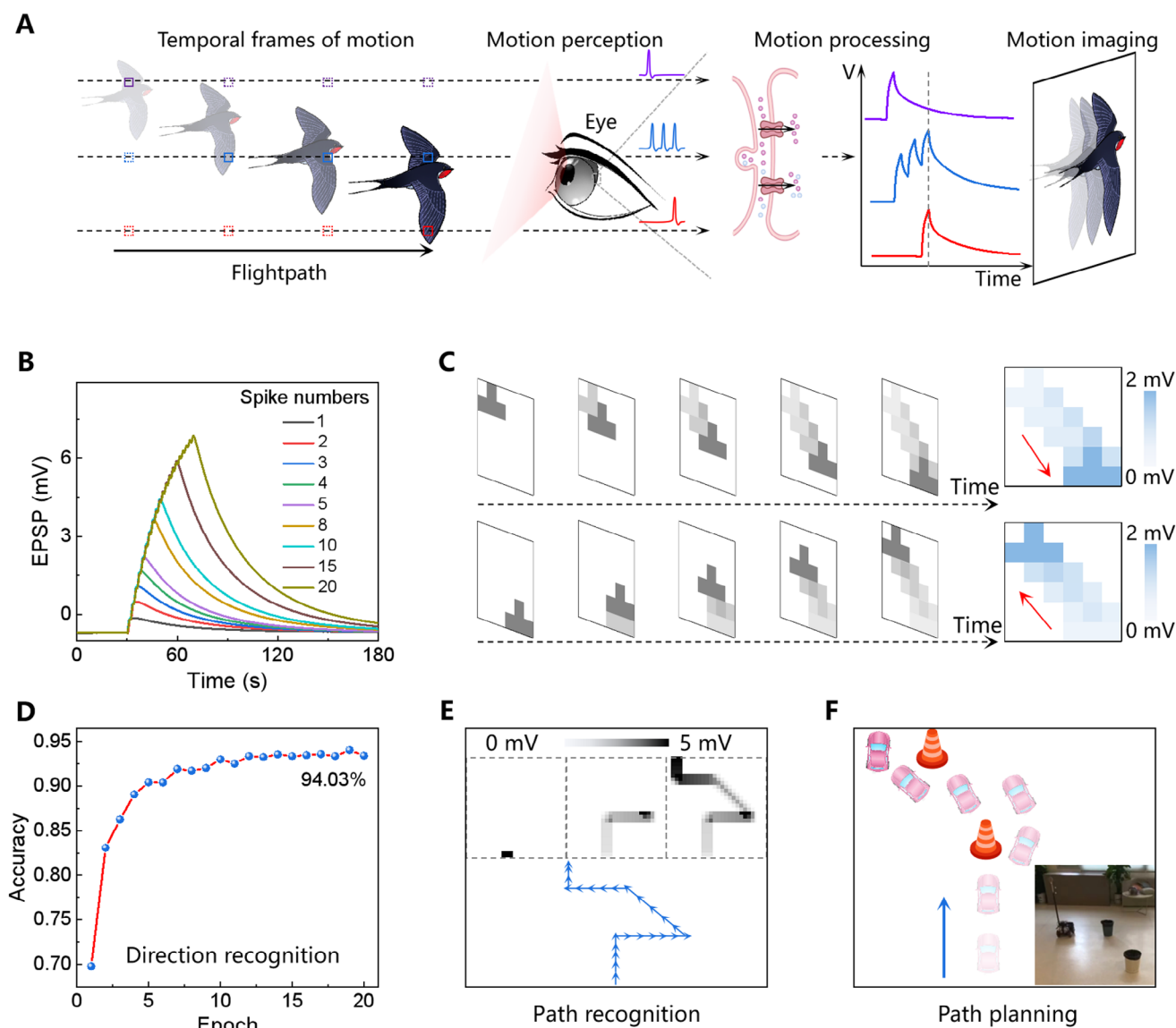


Figure 5. Motion analysis and path planning. A) The human visual system efficiently recognizes and understands motion information by perceiving sequential visual sequences and processing them into a time-compressed state via synapses. B) Spike-number dependent plasticity of the excitatory hydrogel artificial synapse. C) Recognition of the motion direction on the device array. D) The direction recognition accuracy. E) Demonstration of specific path recognition. F) Schematic of a robot vehicle planning path, with an inset image showing the optical image of a robot vehicle in motion.

number of pulses increases, the EPSP gradually increases and exhibits good stability, with the relaxation speed slowing down and the relaxation time extending. Each single pulse can be considered as a frame of motion, suggesting that the device can derive the relationship between motion position and the time axis based on the spatiotemporal differences in relaxation properties. A 6×6 excitatory device array was then used to perceive dynamic motion (Figures S28 and S29, Supporting Information). The preparation process is described in detail in Note S2 (Supporting Information). Specifically, five time frames were employed to represent a particular movement, sampled at a frequency of 1 Hz. As the motion progresses, the EPSP induced by the laser stimulus gradually decays over time, with the EPSP of the subsequent frame exceeding that of the previous frame. This temporal de-

cay, combined with the successive integration of frames, allows the unique EPSP levels to encode and integrate spatiotemporal motion information, clearly revealing the entire motion trajectory from top to bottom. Additionally, when the motion direction reverses, the synapse array can detect the reversed trajectory profile (Figure 5C). This capability aligns with the principles of temporal coding and motion integration in visual processing, where the temporal sequence of stimuli and their cumulative effects are crucial for accurately representing and perceiving motion.

The process of real-world object motion direction recognition was then demonstrated. By fitting the relaxation segments of the curves in Figure 5B, a function curve representing EPSP changes over time was obtained, which is correlated with the number of pulses and validated with a 95% confidence interval

($V = (0.0005176t_0 + 0.0001952)e^{\frac{-t}{30.59}} - 0.00002447$, where t_0 represents the number of light pulses, Figure S30, Supporting Information). This feature was then used to construct the synaptic array model for the recognition and classification of dynamic object directions. A 28×28 synaptic array was simulated, with each synapse corresponding to a pixel. A dataset consisting of 20 000 samples representing object motion was created and divided into training and testing sets in an 8:2 ratio, ensuring that the samples in the test set were distinct from those in the training set. Objects were randomly initialized on the array, and their motion was categorized into five classes: up, down, left, right, and stationary, with a 45-degree classification boundary. Using this data, the output voltage signals of the array during object motion were simulated. Subsequently, these signals were used to train a five-layer multilayer perceptron neural network (Figure S31, Supporting Information). After 20 training epochs, a classification accuracy of 94.03% was achieved by the model (Figure 5D). The kinetics of EPSP decay over time enable the sensor to directly process and generate spatiotemporal information internally, which can be stored in parallel in each pixel in real-time. This greatly enhances data processing efficiency and helps simplify system design.

Path analysis was further explored by using a simulated array of excitatory devices. Initially, we captured the current signal state by sampling the signals generated as a block moved across the array. These signals were analyzed using relaxation functions and a set sampling rate, allowing us to infer the block's movement path. This method simulates real-world scenarios, such as path planning in vehicle motion. By precisely tracking changes in synaptic device activity triggered by the movement of the block, the object's path in space was reconstructed (Figure 5E). The obtained path was represented as a 28×28 grid map. In this map, path planning regions were denoted by non-zero values, while the rest of the area was represented by zero. Since the trajectory was represented as an area rather than a single curve, the map was first binarized (non-zero values were set to 1). An erosion operation was then applied to the trajectory region to shrink and convert it into a curve. To simplify the control of the robot vehicle, eight possible movement directions were defined (top-left, top, top-right, right, bottom-right, bottom, bottom-left, and left). After establishing the initial position of the robot vehicle, its motion was guided according to the position of the processed curve, enabling effective path planning (Figure 5F; Movie S6, Supporting Information). This method offers biomimetic solutions for developing advanced path planning strategies in autonomous driving systems.

3. Conclusion

In conclusion, ion transport behavior can be well controlled by regulating the ionic interfacial energy barrier of various hydrogel structures, thereby realizing the negative and positive regulation of the optical signal. The inhibitory and excitatory artificial synapses have been developed with a wide range of optical responses and optically tunable synaptic plasticity. They can respond differently according to the intensity and frequency of the laser, thereby optimizing signal processing and perception, which is similar to the retinal light perception mechanism of the

human eye under different lighting conditions. Based on the artificial synapse, we developed convolutional kernels to achieve edge detection and noise reduction, effectively improving the accuracy of image recognition. In addition, due to the relaxation effect of ionic potentials, a visual processing platform fabricated with excitatory hydrogel artificial synapses can realize motion direction recognition and path analysis for bio-inspired retina, which was further used to guide robot vehicles for path planning. The bio-inspired retina, achieved by regulating ion-confined transport, presents a new paradigm for neuromorphic visual information processing. This innovative approach capitalizes on the inherent advantages of ionic devices, whose interdisciplinary nature facilitates seamless integration with cutting-edge developments in neuroscience, advanced materials science, and modern electronics, thereby significantly expanding their potential application. However, critical challenges remain in terms of material stability under operational conditions, system integration complexity, and long-term reliability, requiring further breakthroughs.

4. Experimental Section

Materials: Acrylamide (AAM), polyvinyl alcohol (PVA), LiCl, and 2-hydroxy-2-methylpropiophenone (HMPP) were purchased from Aladdin, N,N'-methylenebisacrylamide (MBAA) was purchased from Sigma-Aldrich, CNT was purchased from Nanjing XFANO Materials Tech Co. Ltd. The dialysis bags with a molecular weight cut-off of 3500, were purchased from Shanghai Jinpan Biotech Co., Ltd. ITO/PET was purchased from Shenzhen Bodhi Innovation Technology Co., Ltd.

Synthesis of CNT Solution: The preparation of the CNT solution followed a reported method.^[30] Briefly, CNTs (100 mg) were added to a mixture of sulfuric acid (37.5 mL) and nitric acid (12.5 mL), and then the mixture was sonicated at 60 °C for 6 h. The resulting mixture was centrifuged at 10 000 rpm for 10 min, and the supernatant was discarded. The precipitate was re-dissolved and centrifuged again with deionized water, and the supernatant was discarded. This process was repeated at least three times. The resulting black slurry was placed in a dialysis bag and dialyzed in deionized water for one week to obtain a neutral carbon nanotube aqueous solution. The solution was concentrated using a rotary evaporator. The solution concentration was calibrated by drying a known volume of the solution and weighing the residue. The solution was diluted to achieve the desired concentration of 5 mg mL⁻¹ of CNT solution.

Fabrication of Hydrogel Artificial Synapse Devices: As shown in Figure 1B, the hydrogel artificial synapse comprises two layers of hydrogel sheets (IH₃₀-CNT/IH₃₀) and two ITO/PET flat electrodes on the top and the bottom. Here, "30" denotes the solid content of the hydrogel, specifically the mass percentage of AAM. Synapse devices where the solid content of the hydrogel is the same in both layers function as inhibitory devices, while devices where the solid content of the lower layer exceeds that of the upper layer function as excitatory devices (e.g., IH₃₀-CNT/IH₆₀).

Take the preparation of an inhibitory device as an example. First, two types of ionic hydrogel sheets of IH₃₀ and IH₃₀-CNT were synthesized. For IH₃₀ sheets, 3 g of AAM, 10 mg of MBAA, 50 µL PVA (10 wt.%) were first dissolved in deionized water, then adding 42.4 mg of LiCl, and 50 µL of HMPP and the volume of the solution was precisely controlled to 10 mL, and then the solution was sealed in a transparent self-made mold (Size of the cavity: 0.5 cm × 0.5 cm × 0.4 mm) and irradiated with an ultraviolet light (350 W) for 15 min to obtain IH₃₀ sheets (Size: 0.5 cm × 0.5 cm × 0.4 mm). The synthesis conditions and steps for the IH₃₀-CNT sheets were the same as those for the IH₃₀ sheets, except that an additional 2 mL of CNT solution (5 mg mL⁻¹) was added, after which the solution solvent was precisely controlled at 10 mL. In these syntheses, PVA was used to increase the viscosity of the solution to prevent CNT aggregation. MBAA and HMPP were the cross-linker and photoinitiator, respectively. After that,

the composite hydrogel was obtained by placing IH₃₀-CNT sheets on top of IH₃₀ sheets, and its top and bottom surfaces were each covered with a commercial ITO/PET flat electrode (Thickness: 0.175 mm) for monitoring ionic electrical signals. Finally, to prevent moisture from evaporating, the device was encapsulated using commercial transparent tape.

FEM Simulation: FEM simulations were performed using COMSOL MultiPhysics (version 6.2) to investigate the ion transport in the hydrogel and the heterogeneous interface. For further details, please refer to Note S1 (Supporting Information) for modeling theory and methods.

Characterization and Electrochemical Measurements: Ultraviolet-visible spectra were recorded on a UV-Visible-Near Infrared Spectrometer (lambda 750s). The temperature of the hydrogels was recorded by a FLUKE 30/CN-L25 visible infrared detector. The optical pulses with tunable wavelengths, intensities, and frequencies were generated through a near-infrared light source (808 nm, MDL-III-808, Changchun New Industries, China), visible light source (520 nm, CEL-100HALED), and UV light source (365 nm, CEL-100HALED) with an optical chopper (GCI-73 m, DHC). All photoelectrical measurements were carried out through a multimeter (Keithley DMM7510, Beijing Hanlei Technology Co. Ltd). A Curve Tracer (Beijing Hanlei Technology Co. Ltd) is used for curve analysis and measurement. The optical power density is measured by an optical power meter (CEL-FZ-A, Ceauliout). All electrical and optical measurements were conducted under atmospheric pressure and at room temperature.

Supporting Information

Supporting Information is available from the Wiley Online Library or from the author.

Acknowledgements

This work was financially supported by the National Key Technologies R&D Program of China (Grant No. 2023YFC2415900), Shenzhen Medical Research Fund (B2401005), the National Natural Science Foundation of China (No.22275079 and 22402076), the Science and Technology Development Fund of Macau SAR (FDCT0086/2022/A2 and 0065/2021/A2), Shenzhen Science and Technology Program (KQTD20221101093559017, JCYJ20230807093205011, EF023/ICMS-WRB/2022/SZSTIC), Guangdong Basic and Applied Basic Research Foundation (2024A1515012600), Guangdong Provincial Key Laboratory of Advanced Biomaterials (2022B1212010003), High level of special funds (G03050K002), the China Postdoctoral Science Foundation (2023M731513), and Starting Grant from Southern University of Science and Technology (SUSTech).

Conflict of Interest

The authors declare no conflict of interest.

Author Contributions

H.Z. and S.W. contributed equally to this work. K.X., L.W., R.W., and H.Z. conceived the idea. H.Z., X.Z., S.L., and G.X. performed the experiments related to material preparation and performance testing. Q.L. and S.W. performed experiments related to neuromorphic computing. M.Z. and H.L. performed path planning of the robot vehicles. H.Z. and Y.C. performed the data analysis about the path planning of the robot vehicles. L.W. performed the finite element modeling and theoretical studies of the transport mechanism of ions in hydrogels. H.Z. and S.W. drafted the original manuscript. All authors joined the data discussion and revised the manuscript.

Data Availability Statement

The data that support the findings of this study are available from the corresponding author upon reasonable request.

Keywords

artificial synapses, hydrogels, ion-confined transport, neuromorphic computing, retinas

Received: January 13, 2025

Revised: February 18, 2025

Published online:

- [1] a) F. Liao, Z. Zhou, B. J. Kim, J. Chen, J. Wang, T. Wan, Y. Zhou, A. T. Hoang, C. Wang, J. Kang, J.-H. Ahn, Y. Chai, *Nat. Electron.* **2022**, 5, 84; b) R. E. Miller, T. J. Tredici, Night Vision Manual for the Flight Surgeon, Armstrong Lab, Brooks AFB, TX **1992**.
- [2] T. Euler, S. Haverkamp, T. Schubert, T. Baden, *Nat. Rev. Neurosci.* **2014**, 15, 507.
- [3] B. C. Skottun, J. R. Skoyles, *Schizophr. Bull.* **2011**, 37, 23.
- [4] a) J. Yu, Y. Wang, S. Qin, G. Gao, C. Xu, Z. Lin Wang, Q. Sun, *Mater. Today* **2022**, 60, 158; b) A. Krogh, *Nat. Biotechnol.* **2008**, 26, 195; c) L. Yu, X. Li, C. Luo, Z. Lei, Y. Wang, Y. Hou, M. Wang, X. Hou, *Nano Res.* **2023**, 17, 503.
- [5] J. H. Byrne, *Postsynaptic Potentials and Synaptic Integration in From Molecules to Networks*, Academic Press, Cambridge, Massachusetts **2004**.
- [6] I. Pavlov, A. Scimemi, L. Savtchenko, D. M. Kullmann, M. C. Walker, *Nat. Commun.* **2011**, 2, 199.
- [7] a) L. Mennel, J. Symonowicz, S. Wachter, D. K. Polyushkin, A. J. Molina-Mendoza, T. Mueller, *Nature* **2020**, 579, 62; b) L. Gu, S. Poddar, Y. Lin, Z. Long, D. Zhang, Q. Zhang, L. Shu, X. Qiu, M. Kam, A. Javey, Z. Fan, *Nature* **2020**, 581, 278; c) Z. Long, X. Qiu, C. L. J. Chan, Z. Sun, Z. Yuan, S. Poddar, Y. Zhang, Y. Ding, L. Gu, Y. Zhou, W. Tang, A. K. Srivastava, C. Yu, X. Zou, G. Shen, Z. Fan, *Nat. Commun.* **2023**, 14, 1972; d) Y. Zhou, Z. Sun, Y. Ding, Z. Yuan, X. Qiu, Y. B. Cao, Z. Wan, Z. Long, S. Poddar, S. Kumar, W. Ye, C. L. J. Chan, D. Zhang, B. Ren, Q. Zhang, H. S. Kwok, M. G. Li, Z. Fan, *Sci. Robot.* **2024**, 9, eadi8666.
- [8] G. Zhou, J. Li, Q. Song, L. Wang, Z. Ren, B. Sun, X. Hu, W. Wang, G. Xu, X. Chen, L. Cheng, F. Zhou, S. Duan, *Nat. Commun.* **2023**, 14, 8489.
- [9] G. X. Zhang, Z. C. Zhang, X. D. Chen, L. Kang, Y. Li, F. D. Wang, L. Shi, K. Shi, Z. B. Liu, J. G. Tian, T. B. Lu, J. Zhang, *Sci. Adv.* **2023**, 9, eadi5104.
- [10] a) J. Chen, Z. Zhou, B. J. Kim, Y. Zhou, Z. Wang, T. Wan, J. Yan, J. Kang, J. H. Ahn, Y. Chai, *Nat. Nanotechnol.* **2023**, 18, 882; b) P. Y. Huang, B. Y. Jiang, H. J. Chen, J. Y. Xu, K. Wang, C. Y. Zhu, X. Y. Hu, D. Li, L. Zhen, F. C. Zhou, J. K. Qin, C. Y. Xu, *Nat. Commun.* **2023**, 14, 6736; c) Y. Wang, Y. Gong, S. Huang, X. Xing, Z. Lv, J. Wang, J. Q. Yang, G. Zhang, Y. Zhou, S. T. Han, *Nat. Commun.* **2021**, 12, 5979.
- [11] a) Y. Hou, Y. Ling, Y. Wang, M. Wang, Y. Chen, X. Li, X. Hou, *J. Phys. Chem. Lett.* **2023**, 14, 2891; b) W. Chen, L. Zhai, S. Zhang, Z. Zhao, Y. Hu, Y. Xiang, H. Liu, Z. Xu, L. Jiang, L. Wen, *Science* **2023**, 382, 559.
- [12] a) D. Wang, M. Kvetny, J. Liu, W. Brown, Y. Li, G. Wang, *J. Am. Chem. Soc.* **2012**, 134, 3651; b) P. Robin, N. Kavokine, L. Bocquet, *Science* **2021**, 373, 687; c) A. Marcotte, T. Mouterde, A. Nigues, A. Siria, L. Bocquet, *Nat. Mater.* **2020**, 19, 1057.
- [13] P. Robin, T. Emmerich, A. Ismail, A. Nigues, Y. You, G. H. Nam, A. Keerthi, A. Siria, A. K. Geim, B. Radha, L. Bocquet, *Science* **2023**, 379, 161.
- [14] T. Emmerich, Y. Teng, N. Ronceray, E. Lopriore, R. Chiesa, A. Chernev, V. Artemov, M. Di Ventra, A. Kis, A. Radenovic, *Nat. Electron.* **2024**, 7, 271.
- [15] T. Xiong, C. Li, X. He, B. Xie, J. Zong, Y. Jiang, W. Ma, F. Wu, J. Fei, P. Yu, L. Mao, *Science* **2023**, 379, 156.

- [16] G. Xu, M. Zhang, T. Mei, W. Liu, L. Wang, K. Xiao, *ACS Nano* **2024**, *18*, 19423..
- [17] Z. Zhu, D. W. H. Ng, H. S. Park, M. C. McAlpine, *Nat. Rev. Mater.* **2020**, *6*, 27.
- [18] Z. Lei, P. Wu, *Matter* **2023**, *6*, 429.
- [19] a) S. H. Han, S. I. Kim, M. A. Oh, T. D. Chung, *Proc. Natl. Acad. Sci. USA* **2023**, *120*, 2211442120; b) H. Tian, C. Wang, Y. Chen, L. Zheng, H. Jing, L. Xu, X. Wang, Y. Liu, J. Hao, *Sci. Adv.* **2023**, *9*, eadd6950; c) X. Luo, C. Chen, Z. He, M. Wang, K. Pan, X. Dong, Z. Li, B. Liu, Z. Zhang, Y. Wu, C. Ban, R. Chen, D. Zhang, K. Wang, Q. Wang, J. Li, G. Lu, J. Liu, Z. Liu, W. Huang, *Nat. Commun.* **2024**, *15*, 3086.
- [20] a) B. Amsden, *Macromolecules* **1998**, *31*, 8382; b) J. Li, D. J. Mooney, *Nat. Rev. Mater.* **2016**, *1*, 16071.
- [21] L. Talbot, R. K. Cheng, R. W. Schefer, D. R. Willis, *J. Fluid Mech.* **1979**, *101*, 737.
- [22] E. R. Nightingale, *J. Phys. Chem.* **2002**, *63*, 1381.
- [23] a) S. W. Boettcher, S. Z. Oener, M. C. Lonergan, Y. Surendranath, S. Ardo, C. Brozek, P. A. Kempler, *ACS Energy Lett.* **2020**, *6*, 261; b) Y. Dobashi, D. Yao, Y. Petel, T. N. Nguyen, M. S. Sarwar, Y. Thabet, C. L. W. Ng, E. Scabeni Glitz, G. T. M. Nguyen, C. Plesse, F. Vidal, C. A. Michal, J. D. W. Madden, *Science* **2022**, *376*, 502.
- [24] S. Zhao, W. Ran, Z. Lou, L. Li, S. Poddar, L. Wang, Z. Fan, G. Shen, *Natl. Sci. Rev.* **2022**, *9*, nwac158.
- [25] X. Wang, Y. Lu, J. Zhang, S. Zhang, T. Chen, Q. Ou, J. Huang, *Small* **2021**, *17*, 2005491.
- [26] X. Wan, T. Tsuruoka, K. Terabe, *Nano Lett.* **2021**, *21*, 7938.
- [27] W. K. Stell, A. T. Ishida, D. O. Lightfoot, *Science* **1977**, *198*, 1269.
- [28] M. C. Morrone, J. Ross, D. C. Burr, R. Owens, *Nature* **1986**, *324*, 250.
- [29] G. Cohen, S. Afshar, J. Tapson, A. van Schaik, in *2017 Int. Joint Conf. on Neural Networks (IJCNN)*, IEEE, Piscataway, NJ **2017**.
- [30] R. Du, J. Wu, L. Chen, H. Huang, X. Zhang, J. Zhang, *Small* **2014**, *10*, 1387.